ADVANCED FUNCTIONAL MATERIALS
www.afm-journal.de

High Hole Mobility and Thickness-Dependent Crystal Structure in α,ω-Dihexylsexithiophene Single-Monolayer Field-Effect Transistors

*Ehren M. Mannebach, Josef W. Spalenka, Phillip S. Johnson, Zhonghou Cai, F. J. Himpsel, and Paul G. Evans**

Monolayer-thickness two-dimensional layers of α,ω-dihexylsexithiophene (α,ω-DH6T) exhibit field-effect hole mobility of up to 0.032 $cm^2 V^{-1} s^{-1}$, higher than previously reported for monolayers of other small-molecule organic semiconductors. In situ measurements during deposition show that the source-drain current saturates rapidly after the percolation of monolayer-high islands, indicating that the electrical properties of α,ω-DH6T transistors are largely determined by the first molecular monolayer. The α,ω-DH6T monolayer consists of crystalline islands in which the long axes of molecules are oriented approximately perpendicular to the plane of the substrate surface. In-plane lattice constants measured using synchrotron grazing-incidence diffraction are larger in monolayer-thickness films than the in-plane lattice constants of several-monolayer films and of previously reported thick-film structures. Near-edge X-ray absorption fine structure spectroscopy (NEXAFS) reveals that the larger in-plane lattice constant of single-monolayer films arises from a larger tilt of the molecular axis away from the surface normal. NEXAFS spectra at the C 1s and S 2p edges are consistent with a high degree of molecular alignment and with the local symmetry imposed by the thiophene ring. The high mobility of holes in α,ω-DH6T monolayers can be attributed to the reduction of hole scattering associated with the isolation of the thiophene core from the interface by terminal hexyl chains.

1. Introduction

Optimizing the structural and chemical properties of organic semiconductors has the potential to lead to important improvements in the performance and versatility of organic electronic devices. A significant challenge arises because the charge accumulation layers of organic field-effect transistors (OFETs) have typical thicknesses of only a few planes of molecules.[1,2] The layer of material responsible for charge transport is therefore far thinner than the typical total thickness of the organic semiconductor materials film in these devices. One consequence of this mismatch is that functioning FETs can be readily fabricated using organic semiconductor layers with monolayer-scale thicknesses, rather than the tens or hundreds of nanometers of conventional devices.[1–3,4] The mobility of holes in monolayer transistors, however, can be orders of magnitude lower than in devices several molecular layers thick, as is observed, for example, in monolayer-scale pentacene transistors.[5,6]

The low mobility of holes in monolayer devices arises from a combination of molecular-scale and microstructural effects. Charge carriers are trapped or scattered by defects and impurities in the accumulation region or at its interfaces. In addition, at such small thicknesses, due to the small size of the crystal and the proximity of the gate insulator interfaces, monolayers of small-molecule organic semiconductors have a complex arrangement of molecules, often including different island morphologies and crystallographic structures than in thicker films.[7,8] The crystallographic differences lead to different intrinsic overlap of the molecular orbitals of adjacent molecules and thus to different hole transport characteristics.[9] Finally, differences in the sizes of crystals can lead to large changes in the average mobility due to the geometric change in the relative contribution of scattering at grain boundaries.[10] These effects combine to place monolayer-scale FET devices in a different regime of organic semiconductor materials science than devices based on thicker layers. As a result, new strategies must be evolved for the selection of monolayer semiconducting materials. The

E. M. Mannebach, Prof. P. G. Evans
Department of Materials Science and Engineering
University of Wisconsin-Madison
Madison, WI 53706, USA
E-mail: evans@engr.wisc.edu
J. W. Spalenka
Materials Science Program
University of Wisconsin-Madison
Madison, WI 53706, USA
P. S. Johnson, Prof. F. J. Himpsel
Department of Physics
University of Wisconsin-Madison
Madison, WI 53706, USA
Dr. Z. Cai
Advanced Photon Source
Argonne National Laboratory
Argonne, IL 60439, USA

DOI: 10.1002/adfm.201201548

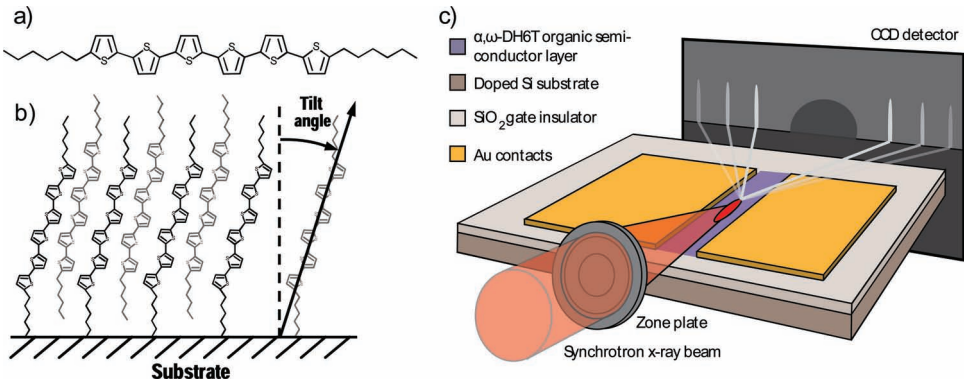

Figure 1. a) Molecular structure of α,ω-dihexylsexithiophene (α,ω-DH6T). b) Proposed arrangement of α,ω-DH6T molecules on SiO_2. The molecular tilt is defined as the average angle between the long axes of the thiophene core of the molecule and the surface normal. c) Schematic of the synchrotron GIXD experiment.

low mobility of charge carriers in monolayers of organic semiconductors presents an opportunity to use the molecular and crystallographic design of materials to reduce the gap between monolayers and conventional thin film devices.

The structures of pentacene and similar organic semiconductors exacerbate the problem of forming monolayers exhibiting high charge-carrier mobility. The orbitals responsible for semiconducting properties extend across the entire molecule, making monolayer films quite sensitive to the interface between the organic semiconductor and the gate dielectric. One way to mitigate this effect is to separate the semiconductor core of the molecules from the gate insulator interface either via additions to the molecules[11] or by chemically attaching an interfacial monolayer to gate insulator.[10] Adding long alkyl chains to semiconductor oligomers, for example, can isolate the conjugated core from electronic traps on the dielectric surface.[11,12] The alkyl chains also facilitate long-range ordering and the creation of mesophases in crystalline films due to strong lipophilic-hydrophobic interactions.[13–15] Alkyl-substituted oligomers such as α,ω-dihexylsexithiophene (α,ω-DH6T), shown in **Figure 1** a, are thus promising for monolayer-scale organic electronics because the alkyl chains both reduce the effect of interfacial traps by screening charge carriers from the dielectric interface and promote crystallinity by increasing the strength of intermolecular interactions between the conjugated cores.

Oligothiophenes and their alkyl- or styryl- substituted derivatives are chemically and electrically stable in air.[13,16] Previous investigations of the alkyl-substituted derivative have made use of the increase in solubility introduced by the terminal alkyl chains, which facilitates the creation of thin films by solution processing.[17] The mobility of holes in α,ω-DH6T OFETs using SiO_2 gate insulators ranges from 10^{-4} to 5×10^{-2} cm^2 V^{-1} s^{-1}.[13–15,18–23] The mobility can be improved to 0.16 cm^2 V^{-1} s^{-1} by introducing an octadecyltrichlorosilane (OTS) monolayer on the SiO_2 before depositing the α,ω-DH6T, consistent with the expectation that increased isolation from interface traps enhances the hole mobility.[18] Here, we show that OFET devices based on monolayer-thickness films of α,ω-DH6T can exhibit hole mobility up to 0.032 cm^2 V^{-1} s^{-1}, on the order of the highest previously reported mobility for α,ω-DH6T on non-functionalized SiO_2, equivalent to highly crystalline thiophene-oligomer monolayers attached via a chemical anchoring group,[12] and more than three times the highest previously reported mobility for vacuum-deposited monolayer films of any organic semiconductor.[2,6,11] In addition, the magnitude of the threshold voltages in α,ω-DH6T monolayers we describe here is far lower than previously reported for pentacene monolayer transistors.[2] The higher mobility and lower threshold voltage for α,ω-DH6T monolayers in comparison with previous monolayers of other small-molecule organic semiconductors are consistent with the improved isolation and crystallinity provided by the α,ω-DH6T alkyl chains.

Crystallographic information regarding the structure of thin films of α,ω-DH6T on SiO_2 with thicknesses in the monolayer to several-monolayer regime is not yet available. At far larger film thicknesses, micrometer-thick α,ω-DH6T films on SiO_2 have crystal structures that consist of layers of α,ω-DH6T molecules in which the long axes of the molecules are nearly parallel to the surface normal and in which the molecules are arranged in a herringbone motif within a monoclinic unit cell.[13] Interestingly, it has been observed in the case of sexithiophene deposited on TiO_2 that the order or disorder of the underlying structure can cause significant changes in the orientation, growth, and electronic properties of the sexithiophene layers.[24] Individual molecules and monolayer films of α,ω-DH6T on metals[25–29] and highly-ordered pyrolytic graphite[30] have structures in which the long axis of the α,ω-DH6T molecule lies in the plane of the substrate surface. This structure persists for the first several monolayers.[25–30] We expect, however, that on insulating surfaces the interaction of the π-orbitals with the substrate will be much weaker, favoring an orientation with the long axis of the molecule near the surface normal, as is observed in thicker films.[13] The expected upright arrangement of molecules is shown in Figure 1b with geometric definitions of the key parameters of the structure, as used in the analysis of the experiments described below. We show using atomic force microscopy (AFM), synchrotron grazing-incidence X-ray diffraction (GIXD) studies of the channel of OFET devices as in Figure 1c, and near edge X-ray absorption fine structure (NEXAFS) spectroscopy that the structure of α,ω-DH6T monolayers is consistent with this upright molecular arrangement.

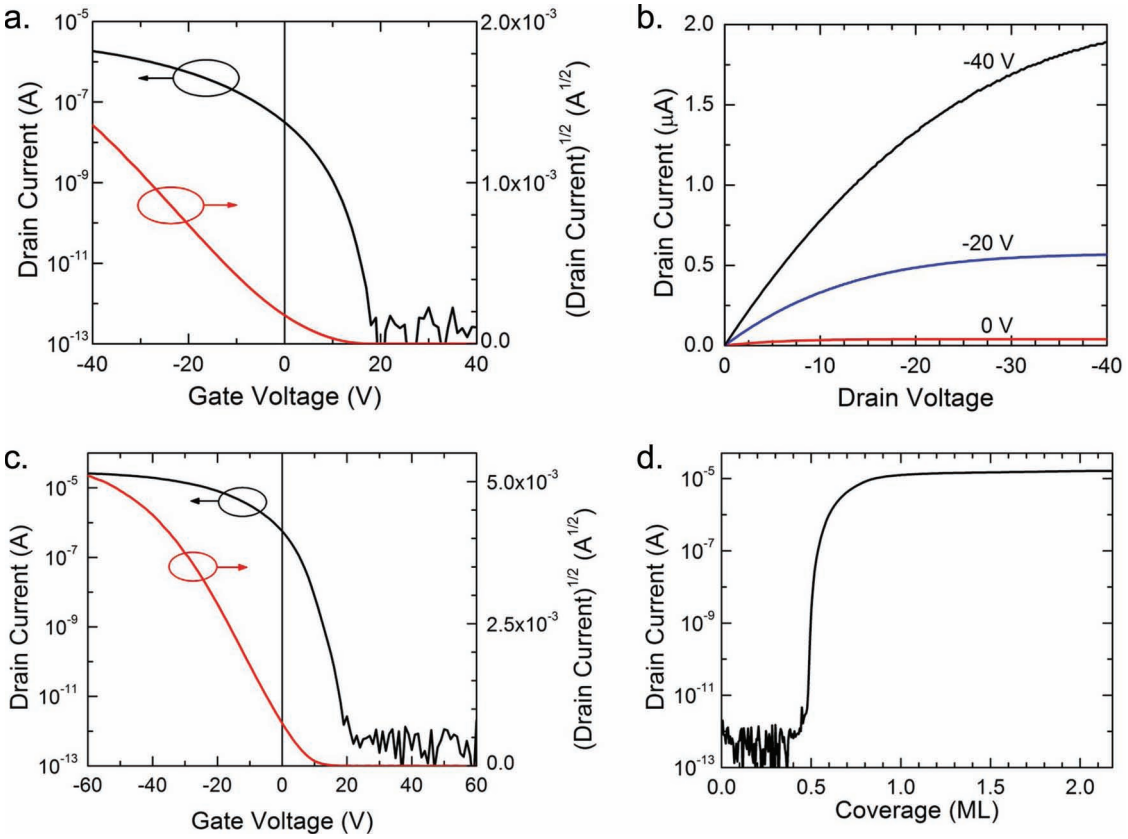

Figure 2. Electrical characteristics of a α,ω-DH6T single-monolayer OFETs. a) Transfer curve acquired with $V_D = -30$ V. A linear fit to $(I_{DS})^{1/2}$ in the range of 0 V ≤ V_G ≤ –40 V was used to calculate the field-effect mobility of the devices. b) Output curves of the same device. c) Current-voltage characteristics of a device with an α,ω-DH6T coverage of 1.3 ML and field-effect mobility of 0.032 cm^2 V^{-1} s^{-1}. d) In situ measurement of I_{DS} during the growth of an α,ω-DH6T film of several monolayer thickness at $V_G = -80$ V and $V_D = -50$ V.

We further find that the two-dimensional crystal lattice of the α,ω-DH6T monolayer is expanded when compared to thicker films and that this expansion is caused by an increase in the tilt angle between the long axis of the α,ω-DH6T molecule and the surface normal.

2. Results and Discussion

2.1. α,ω-DH6T Monolayer Transistors

Thin-film transistors based on monolayer-scale films of α,ω-DH6T were fabricated and characterized using the methods described in the Experimental Section. The α,ω-DH6T OFETs exhibit *p*-channel enhancement mode current-voltage characteristics. A transfer curve, i.e., the variation of the drain current I_{DS} as a function of gate voltage V_G at constant drain voltage V_D, is shown for a representative α,ω-DH6T monolayer OFET in **Figure 2** a. The output curves corresponding to the variation of I_{DS} as a function of V_D at a series of different gate biases V_G for the same transistor appear in Figure 2b. The α,ω-DH6T transistor for which the curves are shown in Figure 2 had a threshold voltage $V_T = 4.4$ V. Values of V_T for several transistors ranged from –3.6 V to +14 V, with no variation as a function of molecular coverage. The magnitude of the threshold voltage of α,ω-DH6T monolayer OFETs is far smaller than in previous pentacene monolayers, where V_T reached several tens of volts at monolayer coverage.[2] Threshold voltages with similarly small magnitudes have been observed in other thin thiophene layers.[11,12,16] These smaller values of V_T for α,ω-DH6T transistors are consistent with the isolation of the semiconducting core from interfacial traps.

The field-effect mobility, μ_{eff}, of holes in α,ω-DH6T was calculated in the saturation regime using:

$$I_{DS} = \frac{WC_i}{2L}(V_G - V_T)^2 \mu_{eff} \quad (1)$$

In Equation 1, C_i is the capacitance per unit area of the SiO_2 dielectric (164 pF mm^{-2}), and W and L are the width and length of the channel, respectively. The device for which the electrical measurements are shown in Figure 2a,b has L = 30 μm and W = 1000 μm. The DH6T layer was deposited with a substrate temperature of 70 °C. The slope of the linear part of the plot of $I_{DS}^{1/2}$ vs V_G, as in Figure 2a, was used to calculate μ_{eff}. Individual α,ω-DH6T monolayer OFETs have values of μ_{eff} ranging from 2.8 × 10^{-3} cm^2 V^{-1} s^{-1} to as high as 0.032 cm^2 V^{-1} s^{-1}. The mobility of holes in the OFET for which the electrical characteristics are shown in Figure 2a,b is 4.5 × 10^{-3} cm^2 V^{-1} s^{-1}. The current-voltage characteristics of the device exhibiting the

highest mobility of 0.032 $cm^2\ V^{-1}\ s^{-1}$ are shown in Figure 2c. This device had a total DH6T coverage of 1.3 ML, channel length and width of 25 and 1000 μm, respectively, and was grown at a substrate temperature of 40 °C.

The α,ω-DH6T OFETs exhibited high hole mobility only when the SiO_2 surface was processed prior to the deposition of organic semiconductor using an ultraviolet-ozone cleaning step. Despite the additional pre-cleaning of the surface, device-to-device variation of the electrical properties remained even after these procedures. The cause for remaining variation is unknown.

2.2. Channel Formation in Monolayer Devices

In situ electrical measurements were conducted during the growth of the α,ω-DH6T layers in order to examine the relationship between formation of functioning OFETs and the microstructure of the thin film. The drain current I_{DS} was measured during growth with V_G and V_D held at –80 and –50 V, respectively. The variation of the drain current as a function of the coverage of α,ω-DH6T are shown in Figure 2d for a sample grown with a substrate temperature of 70 °C. The key features are an initially negligible current associated with gate leakage followed by an abrupt increase to more than 10 μA upon the percolation of monolayer-high islands. A rapid increase of I_{DS} is also observed at the percolation threshold during the deposition of monolayer-scale pentacene transistors.[2] The conversion between elapsed deposition time and the instantaneous coverage of α,ω-DH6T was performed using AFM measurements of the final molecular coverage.

The saturation of the source-drain current at a single α,ω-DH6T monolayer gives us qualitative insight into defects and traps at the dielectric/organic semiconductor interface. If several monolayers were required for the mobility to reach its maximum value, as is the case in pentacene,[2,5] we would suspect that charge carriers in the first monolayer are not adequately screened from interfacial trap states. In the case of poor screening, additional layers of molecules provide a conduction path around the defects and trap states. The source-drain current in our α,ω-DH6T OFETs saturates as the first monolayer is completed, indicating that nearly all of the current is carried in the first monolayer and that the charge carriers are effectively decoupled from the interface. In pentacene, however, 2 to 6 molecular layers must be deposited before saturation in the current or mobility is observed,[2,5] indicating that the first several pentacene monolayers are affected by the inhomogeneity introduced by interfacial defects and trap states.

The interaction between α,ω-DH6T and SiO_2 favors the formation of single-layer islands. AFM images of α,ω-DH6T films with several different coverages are shown in **Figure 3**. Islands with heights of more than one molecular layer are absent from the images acquired at 0.26 and 0.92 ML, which indicates that the second molecular layer of α,ω-DH6T did not form until after the completion of the first monolayer. The initial nucleation density was 20 islands per μm^2 at the deposition rate of

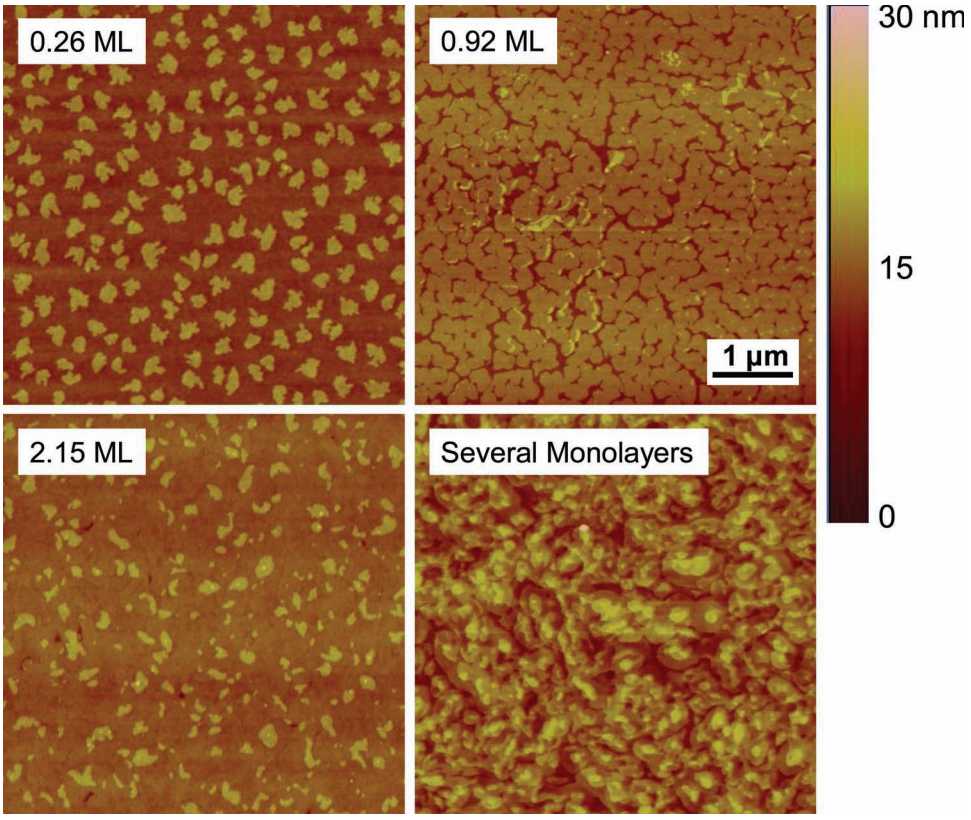

Figure 3. Atomic force microscope images of α,ω-DH6T islands on SiO_2 substrates at several α,ω-DH6T coverages. Identical height and lateral distance scale bars apply to all of the images.

0.07 ML/min used in this study. The lateral extent of islands at monolayer-coverages of α,ω-DH6T was thus approximately 200 nm. Previous monolayer transistors formed from other small-molecule organic semiconductors have had far larger island sizes ranging from 700 nm to several μm.[2,6,11,23] The small island sizes of α,ω-DH6T in comparison with monolayers of other organic semiconductors points to an origin of the increased mobility other than the geometric reduction of grain boundary scattering due to a change in island sizes. The AFM images show that monolayer-high islands in the first layer of α,ω-DH6T have heights of 3.5 nm. Islands of subsequent layers have step heights of 3.7 nm.

2.3. Crystallographic Structure of Monolayer and Several-Monolayer Films

Synchrotron GIXD studies of α,ω-DH6T thin films were conducted to probe the crystallographic structure of α,ω-DH6T in the monolayer thickness regime. Figure 1c shows a schematic of the experimental arrangement in which the X-ray beam was focused using a Fresnel zone plate so that the entire footprint of the beam fell within the channel of an OFET. The focused X-ray beam covered many α,ω-DH6T islands. Because the crystal structure within each island is randomly oriented in the plane of the surface, the resulting distribution of scattered X-ray intensity is a two-dimensional powder diffraction pattern consisting of rods of intensity extending along the surface normal. Similar diffraction patterns have been observed for pentacene monolayers.[7,31] Experimental details of the X-ray diffraction study are given in the Experimental section.

Figure 4 a shows diffraction patterns acquired from monolayer and several-monolayer α,ω-DH6T thin films. The diffraction patterns are analyzed using the plots of the intensity as a function of the in-plane momentum transfer q_{xy}, obtained by integrating the diffraction pattern along the out-of-plane angular direction, as shown in Figure 4b. Here, we define q_{xy} to be $\frac{4\pi}{\lambda}\sin\theta_d$, where θ_d is half of the angle between the observed reflection and the direction of the incident X-ray beam direction, and λ is the X-ray wavelength. The broad feature centered at $q_{xy} = 1.3$ Å^{-1} arises from the SiO_2 gate dielectric layer, and the faint ring at $q_{xy} = 2.32$ Å^{-1} in the monolayer diffraction pattern is due to the illumination of indium solder on the source and drain electrodes by a tail of the focused X-ray beam. The peak intensities of the X-ray reflections from the several-monolayer sample factor of 15 more intense than the monolayer, consistent with the difference in thickness between the two layers.

Bragg reflections in the single-monolayer diffraction pattern appear at lower q_{xy} than reflections in the several-monolayer pattern, indicating that the two-dimensional lattice of the monolayer is expanded with respect to the several-monolayer film. Two-dimensional indices of the reflections in Figure 4 are given under the assumption of a two-dimensional unit cell with monoclinic symmetry. Lattice parameters calculated using a least-squares fit to the peak wavevectors are shown in **Table 1**. The lattice parameters of both the monolayer and several-monolayer films are expanded with respect to the values reported for micrometer-thick α,ω-DH6T films on SiO_2.[13]

Table 1. Lattice parameters for α,ω-DH6T films of monolayer and several-monolayer thicknesses based on the present work, and for bulk-like thickness after Ref.[13]

Film Thickness	a [Å]	b [Å]	γ [deg.]
Monolayer	6.29	8.91	90.0
Several Monolayers	5.93	8.38	89.2
Bulk[13]	5.88	7.88	90.0

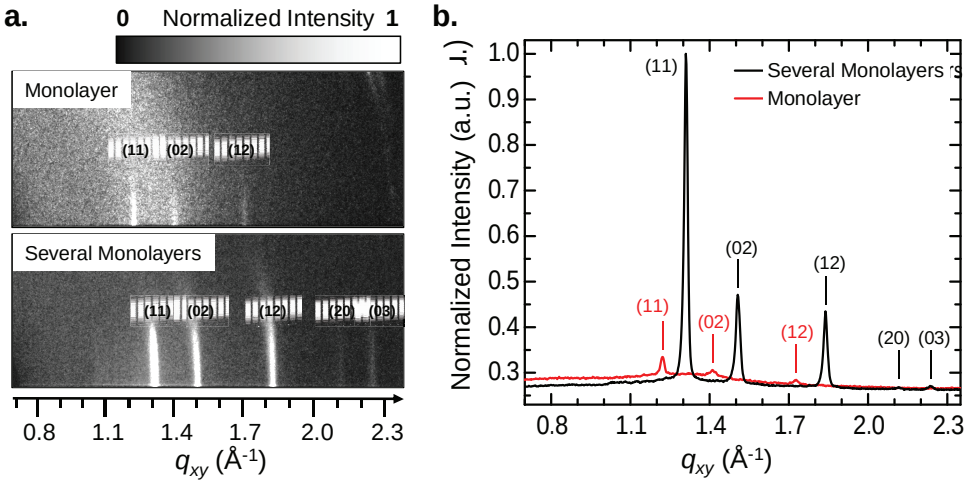

Figure 4. Diffraction patterns for monolayer and several-monolayer α,ω-DH6T films on SiO_2. a) A 0.92 ML film (top) and a film with a thickness of 25 nm (several monolayers, bottom). The {11}, {02}, and {12} Bragg rods are visible in both patterns. The {20} and {03} rods are visible in the diffraction pattern for the thicker sample but not for the monolayer. The broad feature near 1.3 Å^{-1} is due to diffuse scattering from the SiO_2 substrate. A faint ring at 2.32 Å^{-1} corresponds to powder diffraction from In solder on the Au electrodes. b) Integrated intensity in the diffraction pattern as a function of q_{xy}. The intensities in both diffraction patterns were normalized to the strongest peak in the diffraction pattern of the thicker sample. The shifting of the monolayer peaks to lower q_{xy} indicates an expansion of the two-dimensional crystal lattice.

2.4. Electronic Structure at the C Atoms

Near edge X-ray absorption fine structure (NEXAFS) spectroscopy was used to investigate the orientation of α,ω-DH6T molecules in monolayer and several-monolayer films. NEXAFS spectra are sensitive to the relative orientation of the molecular orbitals with respect to the polarization of the incident soft X-ray beam. The tilt angle, defined here as the angle between the substrate surface normal and the long axis of the rigid thiophene core, as in Figure 1b, can be extracted from a series of spectra acquired at different angles of incidence of the X-ray beam. An increase in the tilt angle of the α,ω-DH6T molecules from the substrate surface normal is found in α,ω-DH6T monolayers, consistent with the expansion of the two-dimensional crystal lattice monolayer thicknesses. NEXAFS measurements were conducted at both the C 1s and S 2p absorption edges in order to obtain element-specific information about the character of the unoccupied orbitals.

Figure 5 shows the C 1s absorption spectra for a monolayer and for a several-monolayer film of α,ω-DH6T at a series angles of incidence of the linearly-polarized soft X-rays. The spectra in Figure 5 exhibit fine structure, similar to what has been previous X-ray absorption spectra of thin layers of sexithiophene and thiophene derivatives,[32,16] visible because of the high degree of crystalline order in the sample. The X-ray angle of incidence is measured from the surface normal, and is arbitrarily assigned a positive or negative sign, depending on the azimuthal direction. The spectra have been normalized to the C 1s continuum far above threshold (at 318 eV), where the absorption becomes nearly independent of the polarization. Peaks in the absorption spectrum arise from transitions from the C 1s level into empty π* orbitals. The energies and symmetries of these transitions can be analyzed using reported calculations of the electronic structure of a single thiophene molecule[24,25] and of a chain of six thiophene molecules.[33,34] As shown in the inset at the bottom of Figure 5, the interaction between the B_1 orbitals is much stronger than for the A_2 orbitals,[34] which leads to a much wider manifold. The peak assignments indicated in Figure 5 are compatible with the polarization selection rules, which are given in Section 2.6.

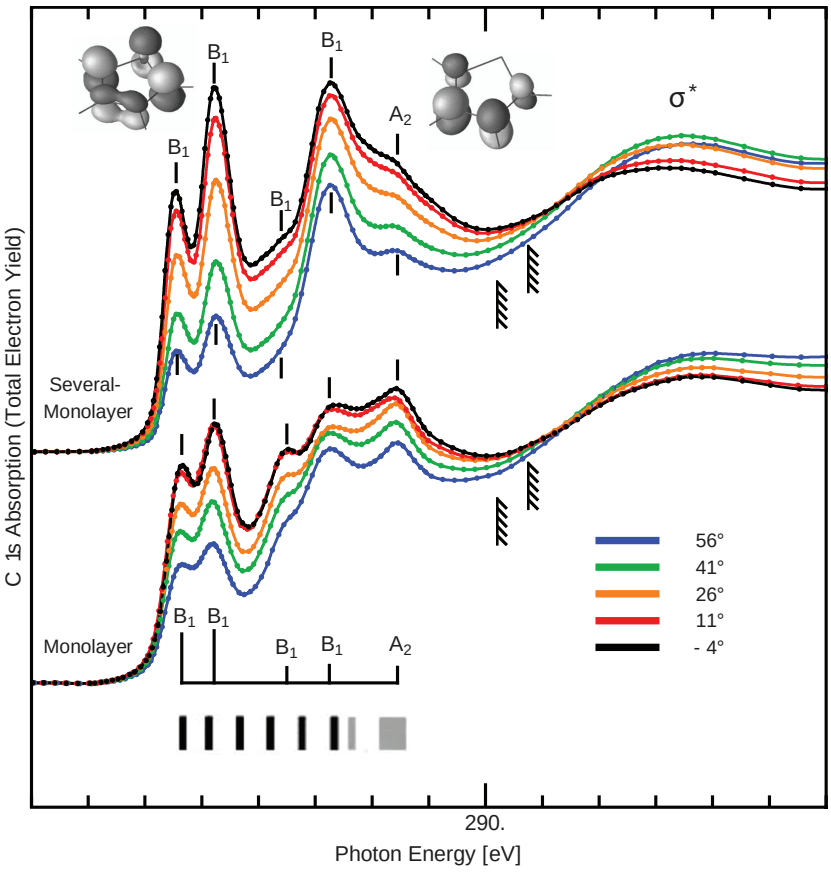

Figure 5. Angle-dependent C 1s absorption spectra of monolayer and several-monolayer α,ω-DH6T thin films. Molecular orbital assignments are based on their polarization dependence and literature results for a single thiophene molecule.[28,34] Hatched lines indicate the ionization potentials of carbon along the conjugated backbone (higher energy) and along the base of the thiophene ring (lower energy). The bottom inset shows the energy levels for the B_1 (black) and A_2 (gray) unoccupied orbitals for a chain of six thiophenes, after Ref.[34] The B_1 levels spread out much more in energy due to stronger coupling between thiophene molecules. Representations of the molecular orbitals of thiophene are reproduced with permission.[28] Copyright 2000, Elsevier.

In addition to the final-state splitting, there is an initial-state splitting caused by the two inequivalent C atoms. Their two ionization potentials are indicated by hatched lines in Figure 5, for which the energies are taken from bithiophene.[28,25] Carbon atoms bonded to S have a higher ionization potential than C atoms at the base of the thiophene ring. The difference in ionization potentials is due to the withdrawal of negative charge from the neighboring C atoms by the electronegative S atom. The splitting increases from 0.34 eV in thiophene to 0.55 eV in bithiophene,[28] where a C–H bond is replaced by a C–C bond for the C next to S. Replacing the H by the more electronegative C ligand causes an additional withdrawal of negative charge. From the split C 1s level alone one would expect a duplication of all the peaks in the C 1s NEXAFS spectra. That creates an ambiguity whether the line spacing is caused by the two C 1s initial states or by the six B_1 final states (see inset at the bottom of Figure 5). This may be the cause of the uneven intensities of the observed B_1 multiplet.

2.5. Molecular Orientation in the Monolayer and Several-Monolayer Films

There is an exchange of intensity between the π^* and σ^* regions of the C 1s absorption spectra as the incidence angle increases, which reflects the orthogonal orientation of the π- and σ-bonds. The strong angular modulation of the π^* intensity demonstrates that there is a high degree of ordering in both monolayer and thicker films. The tilt angle of α,ω-DH6T molecules

can be determined by fitting the variation in the intensity of the sharp π^* peaks near 285 eV as a function of the angle of incidence. This spectral region is the most useful for determining the tilt angle of the molecules because it contains π^* peaks corresponding to the C atoms that make up the large conjugated π-system of the thiophene core of the molecule. The π^* wave functions have their optical dipole moment normal to the plane of the thiophene rings. In addition, the π^* peaks in this region are sharp and do not shift in energy as the angle of incidence changes.

The orientation of the α,ω-DH6T molecules is determined using a model for the absorption intensity that averages the optical dipole matrix element over the orientation of the molecules in random azimuthal tilt domains.[35] A similar procedure has been used previously to determine the evolution of the molecular tilt angle as a function of the overall layer thickness for pentacene on SiO_2.[36] The magnitude of the absorption I depends on the incident angle θ and molecular orientation α according to:

$$\frac{I(\theta)}{I(\theta=0)} = \frac{1+\frac{1}{2}\left[3\sin^2\theta-1\right]\left[2\cos^2\alpha-1\right]}{1-\frac{1}{2}\left[3\cos^2\alpha-1\right]} \quad (2)$$

As shown in the inset of **Figure 6**, α is the angle between the azimuthally averaged direction of the π^* orbitals and the surface normal. Due to the random orientation of domains within the α,ω-DH6T films, it is impossible to determine the distribution of molecular tilt angle (defined in Figure 1b) of the α,ω-DH6T thin films unambiguously except in the extreme cases of either perfectly vertical or horizontal orientations.[37] However, near these extremes (i.e., near $\alpha = 90°$ or $\alpha = 0°$), one can estimate the orientations within a small uncertainty depending on the value of α. When the long axes of the α,ω-DH6T molecules are nearly along the surface normal, the tilt angle of α,ω-DH6T is given by 90°–α.

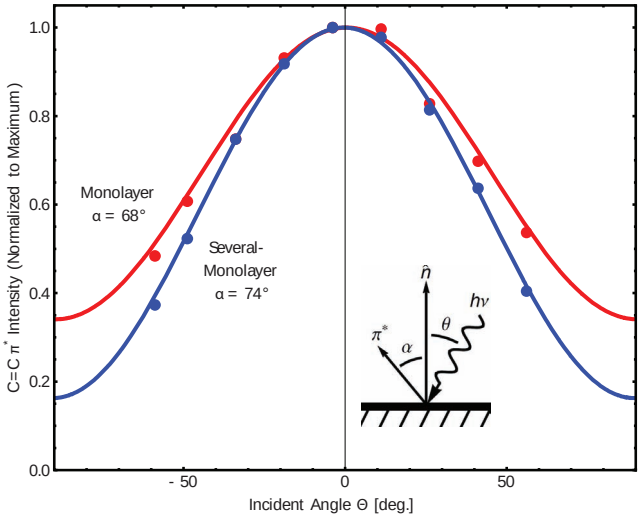

Figure 6. Fits of the integrated absorption in the C = C π^* region from 283 to 286 eV at various angles of incidence using Equation 2. The orientations of the thiophene rings in the monolayer and several-monolayer samples are indicated with the fits. The π^* vector is normal to the thiophene rings and the tilt angle of the long axis of the molecules with respect to the surface normal of the substrate is 90°–α.

Figure 6 shows the incident-angle dependence of the integrated strength of the C 1s-to-π^* absorption spectra in the photon energy region between 283 eV and 286 eV. Results are shown for α,ω-DH6T layers with single monolayer and several monolayer thicknesses. Fits of the model in Equation 2 for the experimental results from the two α,ω-DH6T layer thicknesses are shown as solid lines in Figure 6. The fits yield α = 68° ± 2° for the monolayer and α = 74° ± 2° for the several-monolayer film, where the angular reproducibility contributes ±1° and the assumptions underlying the analysis method in Equation 2 contribute the remaining uncertainty. Since the geometric assumptions affect both samples in the same way, the difference in their orientations is determined reliably. The molecular tilt angles are therefore 22° ± 2° in the monolayer and 16° ± 2° in several monolayers, i.e., the molecules in the thicker sample are more upright than those in the monolayer sample.

Based on the tilt angles, and the molecular length of 3.88 nm reported by Garnier et al.,[13] the NEXAFS results predict heights of molecular steps to be 3.60 nm and 3.73 nm, for monolayers and several-monolayer films, respectively. These step heights are in excellent agreement with the values of 3.5 nm and 3.7 nm observed using AFM. The lower step height we observe here for the first monolayer is also consistent with the larger in-plane lattice constant for α,ω-DH6T monolayers reported in the x-ray diffraction measurements in Table 1. Mauldin et al. have found that the molecular layers of the structurally similar molecules α,ω-distyryl pentathiophene (DS5T) and α,ω-distyryl sexithiophene (DS6T) exhibit the opposite trend, with larger step heights near the interface.[16] We thus suspect that the subtle differences in the molecular crystal structure of the first layers arises from the short-range interaction of the terminal groups with the SiO_2 substrate.

2.6. Electronic Structure at the S Atoms

S 2p spectra are shown in **Figure 7** for films with monolayer and for several-monolayer thicknesses. The spectra are complicated by the splitting of the S 2p level into the S $2p_{1/2}$ and S $2p_{3/2}$ spin-orbit partners. The duplication can be removed by spin-orbit decomposition, since the spin-orbit splitting and intensity ratio are known for the S atom and need to be modified only slightly for S embedded in a molecule. The decomposition makes it possible to extract the dominant S $2p_{3/2}$ contribution to the NEXAFS spectra in Figure 7. By doing this, we remove duplicate peaks from the S $2p_{1/2}$ spin-orbit partner lines together with the angle-dependent energy shifts they cause. The specific method for extracting the S $2p_{3/2}$ contribution is adapted from a previously developed algorithm for decomposing Si 2p in XPS spectra.[38] We use 1.2 eV for the S 2p spin-orbit splitting[39] and 0.49 for the intensity ratio, close to the ratio of 1:2 for the degeneracies of the S $2p_{1/2}$ and S $2p_{3/2}$ energy levels. Before spin-orbit decomposition, each set of polarization-dependent spectra was normalized above the edge at 176 eV, where the polarization dependence has nearly vanished due to the many available final states, analogous to the normalization at the C 1s edge. Hatched lines at 169.9 eV in Figure 7 indicate the ionization energy of the S $2p_{3/2}$ core level.[25]

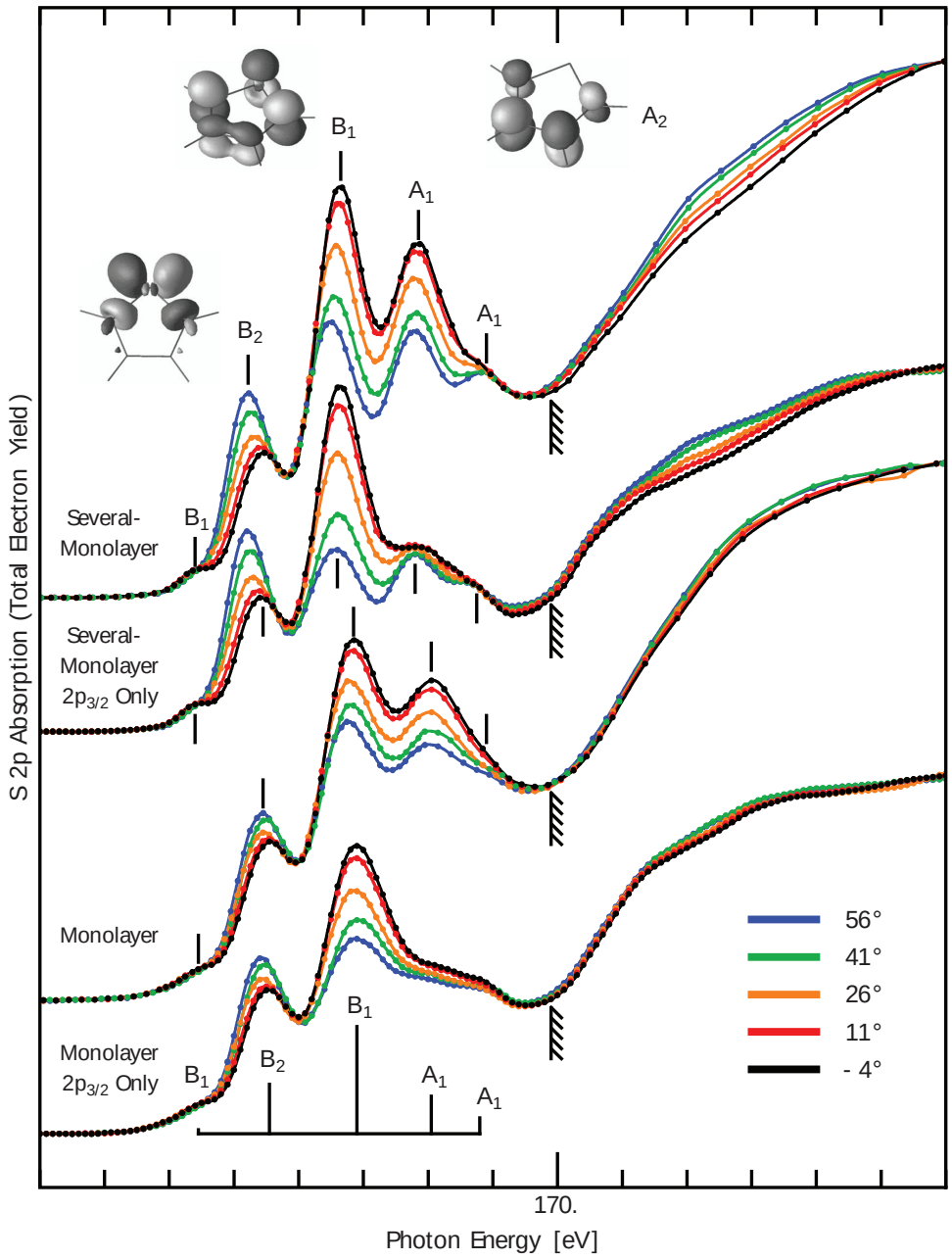

Figure 7. Angle-dependent S 2p absorption spectra of monolayer and several-monolayer α,ω-DH6T films. Molecular orbital assignments are based on the polarization dependence and the experimental spectra of a single thiophene ring given in Ref. [28] The S $2p_{3/2}$ component is isolated to clarify the spectra. When going from a monolayer to several-monolayer films the absorption energies are shifted to lower photon energy by 0.1 to 0.3 eV. The A_2 orbitals are not apparent in the spectra because their wave function has negligible weight at the S atom (see the inset image of the A_2 orbital). Representations of the molecular orbitals of thiophene are reproduced with permission.[28] Copyright 2000, Elsevier.

Compared to the α,ω-DH6T monolayer, the S 2p spectra of the several-monolayer film are shifted to lower photon energy by 0.1 to 0.3 eV. The electron escape depth is in the range of 1 to 10 nm, so electron-yield detection of the absorption process probes the entire monolayer sample but only the top few molecular layers of the thicker sample. Absorption in the deeper layers thus does not contribute to the total electron yield spectra. Interactions between adjacent molecules could also be more prominent in the thicker samples due to potentially higher density of the molecules in each layer.

The molecular orbital assignments in Figure 7 are based on spectra for a single thiophene ring from the literature[24,28,29] and on the symmetry of the transitions determined using polarization selection rules. Like in the C 1s spectra, the S 2p spectra exhibit a strong dependence on the incident angle, again consistent with the high degree of orientation in the α,ω-DH6T

films. The polarization dependence of the peak at 165.6 eV is opposite to that of the higher energy peak at 166.9 eV. This difference indicates that the corresponding unoccupied orbitals are orthogonal to each other, which can be understood by analyzing the local mirror symmetry of the calculated orbitals, as explained below. The result of this analysis suggests B_2 symmetry for the peak at 165.6 eV. A B_2 orbital is indeed obtained for single thiophene in this energy region,[24,25] but has not been included in the DFT calculation for a chain of six thiophene rings.[34]

The optical dipole selection rules for the S 2p core level are more complicated than for the C 1s level. In addition to the dominant $l \rightarrow (l+1)$ channel, which involves transitions from p to d orbitals, we must consider the $l \rightarrow (l-1)$ channel, transitions from p to s orbitals. Furthermore, the analysis of the S absorption spectra must consider the two spin-orbit-split S $2p_{3/2}$ and S $2p_{1/2}$ levels, while the C $1s_{1/2}$ level is not split. As a result, one faces more complicated polarization selection rules at the S 2p edge. A summary of the selection rules is given in **Table 2**.

Instead of using angular momentum selection rules for spherical symmetry, one needs to consider the symmetry of the thiophene molecule. We use the coordinate system defined in **Figure 8**, with *x* out of the plane of the thiophene ring, *z* from the center of the baseline to the apex of the ring, and *y* along the base of the ring, as in the literature.[28] For an allowed optical transition, the dipole matrix element must be even in both *x* and *y*, while no specific parity is required along *z*. The matrix element $M_{fi} = \langle f | \mathbf{A}\cdot\mathbf{p} | i \rangle$ contains the initial state wave function $| i \rangle$, the dipole operator $\mathbf{A}\cdot\mathbf{p}$, and the final state wave function $\langle f |$, each of which has a well-defined parity (see Table 2). Here **A** is the vector potential of the incident X-ray radiation field, which is collinear with the electric field (i.e., the polarization vector of the light), and **p** is the momentum operator. The combined parity of the three factors in M_{fi} must be even for both mirror planes, corresponding to the A_1 representation. Table 2 shows all of the transitions allowed by the two mirror planes of the C_{2v} symmetry group of the thiophene molecule.

Table 2. Dipole selection rules for optical transitions from the C 1s and S 2p core levels in the C_{2v} symmetry of thiophene which contains two orthogonal mirror planes. The allowed transitions are listed by the symmetry of the final state orbitals: A_1 (even in *x*, *y*), A_2 (odd in *x*, *y*), B_1 (odd in *x*, even in *y*), and B_2 (even in *x*, odd in *y*).

Final State	Polarization	Initial State
A_1 (1,z)	z (A_1), y (B_2)	C 1s ($A_1 + B_2$)
	z (A_1)	S $2p_z$ (A_1)
	x (B_1)	S $2p_x$ (B_1)
	y (B_2)	S $2p_y$ (B_2)
A_2 (xy)	x (B_1)	C 1s ($A_1 + B_2$)
	x (B_1)	S $2p_y$ (B_2)
	y (B_2)	S $2p_x$ (B_1)
B_1 (x)	x (B_1)	C 1s ($A_1 + B_2$)
	x (B_1)	S $2p_z$ (A_1)
	z (A_1)	S $2p_x$ (B_1)
B_2 (y)	y (B_2), z (A_1)	C 1s ($A_1 + B_2$)
	y (B_2)	S $2p_z$ (A_1)
	z (A_1)	S $2p_y$ (B_2)

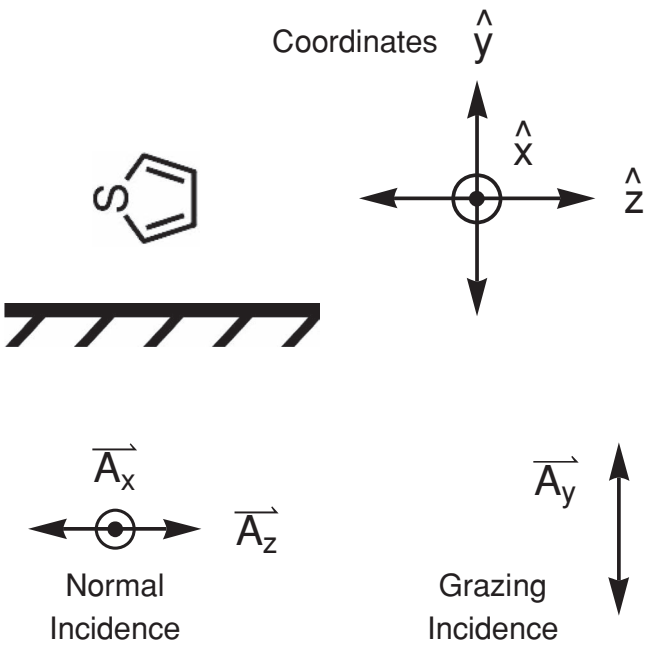

Figure 8. Coordinate assignments for the thiophene molecule. The molecule lies in the *yz*-plane, and it is drawn with an orientation similar to that of adsorbed α,ω-DH6T in Figure 1. The directions of the polarization vectors of the incident photons, $\mathbf{A}_x$, $\mathbf{A}_y$, and $\mathbf{A}_z$, are given for the two extreme cases of normal and grazing incidence. Although the incident soft X-ray beam is linearly polarized, the random azimuthal orientation of α,ω-DH6T in various domains averages over $\mathbf{A}_x$ and $\mathbf{A}_z$ for normal incidence.

The selection rule analysis presented here is the simplest realistic approximation. We have neglected the spin-orbit interaction, which, if included, would require relativistic double groups, whose selection rules are weaker. Therefore the selection rules given in Table 2 should not be considered as strict. In addition, the interaction among the six thiophene molecules in α,ω-DH6T is also neglected. A further caveat stems from the localization of a core hole to a single atom. For the C 1s edge this results in the loss of the mirror symmetry in the y direction, since the C 1s hole will localize either to $+y$ or to $-y$. Only the mirror symmetry in the *x* direction remains, and the symmetry group becomes C_s. However, the S 2p core hole preserves the C_{2v} symmetry. Therefore, we have kept the C_{2v} terminology in Table 2 while taking into account the broken symmetry at the C 1s edge by decomposing the lopsided C 1s hole into a combination of the even A_1 and the odd B_2 representation.[25]

3. Conclusions

Monolayer and several-monolayer films of α,ω-DH6T grown on SiO_2 have room-temperature hole mobility as high as 0.032 $cm^2\ V^{-1}\ s^{-1}$. The hole mobility in these single-monolayers are on the order those previously reported for thick

films of α,ω-DH6T on any substrate and are at least three times higher than the mobility reported for monolayers of any other small-molecule organic semiconductor.[2,11] Using AFM, we find that monolayer and ultra-thin films of α,ω-DH6T on SiO_2 grow as single-molecule-high islands and that the second layer begins to form only upon completion of the first monolayer. Synchrotron GIXD experiments show that the two-dimensional crystal lattice of the monolayer is expanded with respect to the lattices of the thicker samples. This lattice expansion is due to an increase in the tilting of the α,ω-DH6T molecules with respect to the substrate surface normal when the film thickness is limited to one monolayer, as shown by NEXAFS spectroscopy.

The high mobilities of holes in monolayers of α,ω-DH6T are unique in that transistors formed from monolayers of other highly-crystalline organic semiconductors (e.g., pentacene) require several monolayers of semiconducting molecules before the charge carrier mobility saturates. In comparison, the carrier mobility in α,ω-DH6T saturates after the completion of one monolayer. We therefore conclude that the terminal hexyl chains of α,ω-DH6T screen the conducting thiophene core from defects and trap states present at the gate dielectric interface and allow the mobility in α,ω-DH6T films to saturate after completion of the first monolayer. OFETs can thus be fabricated from single-monolayer thickness layers of organic semiconductors instead of the typical tens or hundreds of nanometers used in conventional devices and yet retain useful hole mobilities. Monolayers with optimized structures open the way to far more precisely fabricated organic electronic devices, in which the sizes of the organic semiconductor layers match the fundamental length scale of electronic transport phenomena.

4. Experimental Section

OFETs were fabricated using a bottom-contact configuration. The substrate was a highly-doped *p*-type silicon wafer with a 200 nm thermally grown SiO_2 gate dielectric. Source and drain electrodes consisting of a 70 nm Au film on a 3 nm Cr adhesion layer were deposited via electron beam deposition and patterned using photolithography and lift off. The channel length *L* ranged from 25 to 40 μm for the devices discussed here. The width *W* was 1000 μm for all devices. Substrates were ultrasonically cleaned in acetone, methanol, and deionized water, followed by a 4 min exposure to a UV/ozone lamp. The α,ω-DH6T thin films were grown using vacuum evaporation at a pressure of 10^{-6} Torr (1 Torr = 133.32 Pa) with an effusion cell temperature of 250 °C and substrate temperatures of either 40 or 70 °C. Electrical measurements were performed in situ using an Agilent 4155C semiconductor parameter analyzer connected to the sample using a vacuum feedthrough.

GIXD studies were conducted at station 2-ID-D of the Advanced Photon Source at Argonne National Laboratory using X-rays with a photon energy of 10.1 keV. Diffraction patterns were recorded using a charge-coupled device. The beam was focused to a horizontal spot size of 600 nm using a Fresnel zone plate. The X-ray footprint on the semiconductor channel was highly elongated, on the order of 600 nm wide and several hundred μm long. Exposure times were limited to 2 s using an X-ray shutter in order to eliminate artifacts from X-ray beam damage.

NEXAFS spectra were acquired at the U2 VLS-PGM beamline of the University of Wisconsin Synchrotron Radiation Center (SRC). Radiation damage was minimized by using 5 μm monochromator slits. All absorption spectra were taken using electron detection. The photon energy at the C 1s edge was calibrated using the C = C 1s-to-π* absorption peak at 285.35 eV of graphite as a reference.[40] The S 2p edge was calibrated similarly, using the second order of the grating, where the C 1s-to-π* peak appears at the grating position corresponding to ½ × 285.35 eV = 142.68 eV. The second order C 1s features of C in thiophene cause a more complicated pre-edge background in the S 2p spectra. However, most of this background appears below the S 2p edge and does not affect the S 2p features. The absolute accuracy of the photon energy scale is ±0.2 eV, the relative accuracy between samples is ±0.1 eV, and the relative accuracy between different π* peaks at the same absorption edge is ±0.05 eV. The energy resolution was significantly better than the width of the observed features.

Acknowledgements

This work was supported by the University of Wisconsin Materials Research Science and Engineering Center, National Science Foundation grant number DMR-1121288. Use of the Advanced Photon Source, an Office of Science User Facility operated for the U.S. Department of Energy (DOE) Office of Science by Argonne National Laboratory, was supported by the U.S. DOE under Contract No. DE-AC02-06CH11357. This work is based in part upon research conducted at the Synchrotron Radiation Center at the University of Wisconsin-Madison, which is supported by the National Science Foundation under Award No. DMR-0537588.

Received: June 9, 2012
Revised: August 8, 2012
Published online: September 14, 2012

[1] F. Dinelli, M. Murgia, P. Levy, M. Cavallini, F. Biscarini, D. M. De Leeuw, *Phys. Rev. Lett.* **2004**, *92*, 116802.
[2] B.-N. Park, S. Seo, P. G. Evans, *J. Phys. D: Appl. Phys.* **2007**, *40*, 3506.
[3] A. Shehu, S. D. Quiroga, P. D'Angelo, C. Albonetti, F. Borgatti, M. Murgia, A. Scorzoni, P. Stoliar, F. Biscarini, *Phys. Rev. Lett.* **2010**, *104*, 246602.
[4] A. R. Murphy, J. M. J. Fréchet, *Chem. Rev.* **2007**, *107*, 1066.
[5] R. Ruiz, A. Papadimitratos, A. C. Mayer, C. G. Malliaras, *Adv. Mater.* **2005**, *17*, 1795.
[6] G. Wang, Y. Luo, P. H. Beton, *Appl. Phys. Lett.* **2003**, *83*, 3108.
[7] S. C. B. Mannsfeld, A. Virkar, C. Reese, M. F. Toney, Z. N. Bao, *Adv. Mater.* **2009**, *22*, 2294.
[8] S. Isz, I. Weissbuch, K. Kiaer, W. G. Bouwman, J. Als-Nielsen, S. Palacin, A. Ruaudel-Teixier, L. Leiserowitz, M. Lahav, *Chemistry* **2006**, *3*, 930.
[9] H. Kakuta, T. Hirahara, I. Matsuda, T. Nagao, S. Hasegawa, N. Ueno, K. Sakamoto, *Phys. Rev. Lett.* **2007**, *98*, 247601.
[10] A. Virkar, S. Mannsfeld, J. H. Oh, M. F. Toney, Y. H. Tan, G. Y. Liu, J. C. Scott, R. Miller, Z. Bao, *Adv. Func. Mater.* **2009**, *19*, 1962.
[11] M. Defaux, F. Gholamrezaie, J. Wang, A. Kreyes, U. Ziener, D. V. Anokhin, D. A. Ivanov, A. Moser, A. Neuhold, I. Salzmann, R. Resel, D. M. De Leeuw, S. C. J. Meskers, M. Moeller, A. Mourran, *Adv. Mater.* **2012**, *24*, 973.
[12] E. Smits, S. G. J. Mathijssen, P. A. van Hal, S. Setayesh, T. C. T. Geuns, K. A. H. A. Mutsaers, E. Cantatore, H. J. Wondergem, O. Werzer, R. Resel, M. Kemerink, S. Kirchmeyer, A. M. Muzafarov, S. A. Ponomorenko, B. de Boer, P. W. M. Blom, D. M. de Leeuw, *Nature* **2008**, *455*, 956.
[13] F. Garnier, A. Yassar, R. Hajlaoui, G. Horowitz, F. Deloffre, B. Servet, S. Ries, P. Alnot, *J. Am. Chem. Soc.* **1993**, *115*, 8716.
[14] H. E. Katz, A. Dodabalapur, L. Torsi, D. Elder, *Chem. Mater.* **1995**, *7*, 2238.

[15] J.-H. Kwon, M.-H. Chung, T.-Y. Oh, H.-S. Bae, B.-K Ju, *WASET* **2009**, *31*, 490.
[16] C. E. Mauldin, K. Putambekar, A. R. Murphy, F. Liao, V. Subramanian, J. M. J. Frechet, D. M. DeLongchamp, D. A. Fischer, M. F. Toney, *Chem. Mater.* **2009**, *21*, 1927.
[17] J. A. Rogers, Z. Bao, H. E. Katz, A. Dodabalapur, in *Thin-Film Transistors* (Eds: C. R. Kagan, P. Andry), Taylor and Francis, New York, USA **2003**, pp. 334–378.
[18] H.-S. Seo, Y. Zhang, Y.-S. Jang, J.-H. Choi, *Appl. Phys. Lett.* **2008**, *92*, 223310.
[19] J.-H. Kwon, J.-H. Seo, H. Kang, D. H. Choi, B.-K. Ju, *J. Appl. Phys.* **2007**, *101*, 064502.
[20] H. S. Seo, Y. Zhang, M.-J. An, J.-H. Choi, *Org. Electron.* **2009**, *10*, 1293.
[21] Y. Zhang, H.-S. Seo, M.-J. An, J.-D. Oh, J.-H. Choi, *J. Appl. Phys.* **2011**, *109*, 084503.
[22] F. Garnier, R. Hajlaoui, A. El Kassmi, G. Horowitz, L. Laigre, W. Porzio, M. Armanini, F. Provasoli, *Chem. Mater.* **1998**, *10*, 3334.
[23] M. Kakita, H. Tada, *Mol. Cryst. Liq. Cryst.* **2007**, *471*, 229.
[24] J. Ivanco, T. Haber, J. R. Krenn, F. P. Netzer, R. Resel, M. G. Ramsey, *Surf. Sci.* **2007**, *601*, 178.
[25] S. Duhm, I. Salzmann, N. Koch, H. Fukagawa, T. Kataoka, S. Hosoumi, K. Nebashi, S. Kera, N. Ueno, *J. Appl. Phys.* **2008**, *104*, 033717.
[26] S. Duhm, Q. Xin, N. Koch, N. Ueno, S. Kera, *Org. Electron.* **2011**, *12*, 903.
[27] H. Glowatzki, S. Duhm, K.-F. Braun, J. P. Rabe, N. Koch, *Phys. Rev. B* **2007**, *76*, 125425.
[28] P. Väterlein, M. Schmelzer, J. Taborski, T. Krause, F. Viczian, M. Bassler, R. Fink, E. Umbach, W. Wurth, *Surf. Sci.* **2000**, *452*, 20.
[29] A. P. Hitchcock, J. A. Horsley, J. Stöhr, *J. Chem. Phys.* **1986**, *85*, 4835.
[30] A. Stabel, J. P. Rabe, *Synth. Met.* **1994**, *67*, 47.
[31] S. E. Fritz, S. M. Martin, C. D. Frisbie, M. D. Ward, M. F. Toney, *J. Am. Chem. Soc.* **2004**, *126*, 4084.
[32] D. M. DeLongchamp, Y. Jung, D. A. Fischer, E. K. Lin, P. Chang, V. Subramanian, A. R. Murphy, J. M. J. Fréchet, *J. Phys Chem. B* **2006**, *110*, 10645.
[33] K.-F. Braun, S. W. Hla, *J. Chem. Phys.* **2008**, *129*, 064707.
[34] R. Telesca, H. Bolink, S. Yunoki, G. Hadziioannou, P. Th. Van Duijnen, J. G. Snijders, H. T. Jonkman, G. A. Sawatzky, *Phys. Rev. B* **2001**, *63*, 155112.
[35] J. Stöhr, *NEXAFS Spectroscopy,* Springer, New York, USA **1996**.
[36] F. Zheng, B.-N. Park, S. Seo, P. G. Evans, F. J. Himpsel, *J. Chem. Phys.* **2007**, *126*, 154702.
[37] D. M. DeLongchamp, E. K. Lin, D. A. Fischer, *Proc. SPIE* **2005**, *5940*, 59400A.
[38] F. J. Himpsel, B. S. Meyerson, F. R. McFeely, J. F. Morar, A. Taleb-Ibrahimi, J. A. Yarmoff, in *Core Level Spectroscopy at Silicon Surfaces and Interfaces, Proceedings of the Enrico Fermi School on "Photoemission and Absorption Spectroscopy of Solids and Interfaces with Synchrotron Radiation"* (Eds: M. Campagna, R. Rosei), North-Holland, Amsterdam **1990**, p. 203.
[39] U. Gelius, C. J. Allan, G. Johansson, H. Siegbahn, D. A. Allison, K. Siegbahn, *Phys. Scr.* **1971**, *3*, 237.
[40] E. J. Mele, J. J. Ritsko, *Phys. Rev. Lett.* **1979**, *43*, 68.